

Cohesive fracture and size effect in concrete

L. Cedolin

Politecnico di Milano, Milan, Italy

G. Cusatis

Rensselaer Polytechnic Institute, Troy (NY), USA

ABSTRACT: The classical Hillerborg's "fictitious crack" concept, which consists in a relationship between stress and crack opening displacement, is a simple but very effective model for the simulation of mode I fracture of concrete specimens. Quite problematic, however, appears to be its experimental calibration through direct methods (direct tension tests). For this reason, in the recent past, indirect methods have been proposed. One of the most appealing is the "size effect" method in which the ultimate nominal stress (normalized failure load or structural strength) of specimens of the same geometry but of different sizes, are used to identify the first part of the softening curve. Objective of this paper is to present the results of recent numerical analyses and experimental investigations aimed at the evaluation of the effectiveness of this approach.

1 INTRODUCTION

Fracturing behavior of quasi-brittle materials and, most importantly, the energetic size effect on structural strength cannot be described through the classical Linear Elastic Fracture Mechanics (LEFM) because in quasi-brittle materials the Fracture Process Zone (FPZ) length l_{FPZ} (Fig. 1a) is large compared to the characteristic size D of the structure.

The physical reason for this behavior is the crack bridging effect of material heterogeneities: as fracture propagates stresses can still be transmitted across the crack because the heterogeneities (aggregate pieces in concrete) provide a link between adjacent crack surfaces.

This was clearly recognized by Hillerborg et al. (1976), who proposed that the fracture process zone be modeled through a cohesive (fictitious) crack law characterized by a softening relationship between the cohesive (bridging) stress (σ) and the crack opening displacement (w).

The cohesive law has been traditionally defined by only two parameters: the tensile strength, f_t , which identifies the peak of the curve, and the *total fracture energy*, G_F , defining the total area under the curve (e.g. Hillerborg 1976). More recently it has been observed (Guinea et al. 1992) that, at least within a certain range of characteristic sizes, only the initial part of the softening curve is relevant to the structural performance (structural strength). This part of the softening curve can be efficiently described by the *initial fracture energy*, G_f , which

represents the area under the initial tangent of the softening curve (Fig. 1b).

Size Effect in quasi-brittle materials can be also effectively described through Bažant's Size Effect Law (SEL, Bažant 1984). The SEL can be derived (Bažant & Planas 1998, Bažant 2002) through the use of the Equivalent Linear Elastic Fracture Mechanics (Equivalent LEFM), in which LEFM equations are used with reference to an equivalent crack which consists of the actual stress-free crack (sharp notch or preexisting fatigued cracks) plus a finite length c_f (critical equivalent crack extension or simply crack extension) associated with the size of the FPZ (Fig. 1a).

The cohesive crack approach and the SEL have been widely accepted among researchers and both of them have been extensively used for the simulation of crack propagation and size effect for a large variety of quasi-brittle materials, including concrete. The objective of this paper is to present the results of recent experimental and computational research activity, conducted at the Politecnico di Milano, aiming at the identification of the initial fracture energy, G_f , through the use of methods based on measurements of the structural strength of geometrically similar specimens of different sizes.

2 THEORETICAL ASPECTS

2.1 Bažant's Size Effect Law

With reference to a specimen of notch length $a_0 = \alpha_0 D$, the introduction of the concept of an effective

crack of length a_0+c_f into the LEFM equation for the nominal stress at failure $\sigma_N = K_c[Dg(\alpha_0+c_f/D)]^{-1/2}$ and the subsequent Taylor expansion of the energy release rate $g(\alpha_0+c_f/D) \approx g(\alpha_0)+g'(\alpha_0)c_f/D$ with retention of only the linear term, lead to the well known Bažant's Size Effect Law (SEL) $\sigma_N=[EG_f/(Dg(\alpha_0)+c_f g'(\alpha_0))]^{1/2}$. By using the classical Irwin's equation $K_c^2 = EG_f$, with reference to the initial fracture energy G_f , the SEL can be rearranged in the form

$$\frac{1}{\sigma_N^2} = \frac{g(\alpha_0)}{EG_f} D + \frac{g'(\alpha_0)c_f}{EG_f} \quad (1)$$

The fitting of the experimental results on maximum loads of similar specimens on the basis of Equation 1, performed with a linear regression, leads to the determination of the coefficients a and c of the straight line

$$y = ax + c \quad (1a)$$

from which the values of the fracture energy $G_f = g(\alpha_0)Ea$ and of the crack extension $c_f = cEG_f/g'(\alpha_0)$ can be calculated. The slope a governs the value of G_f and the intercept at the origin c determine the parameter c_f .

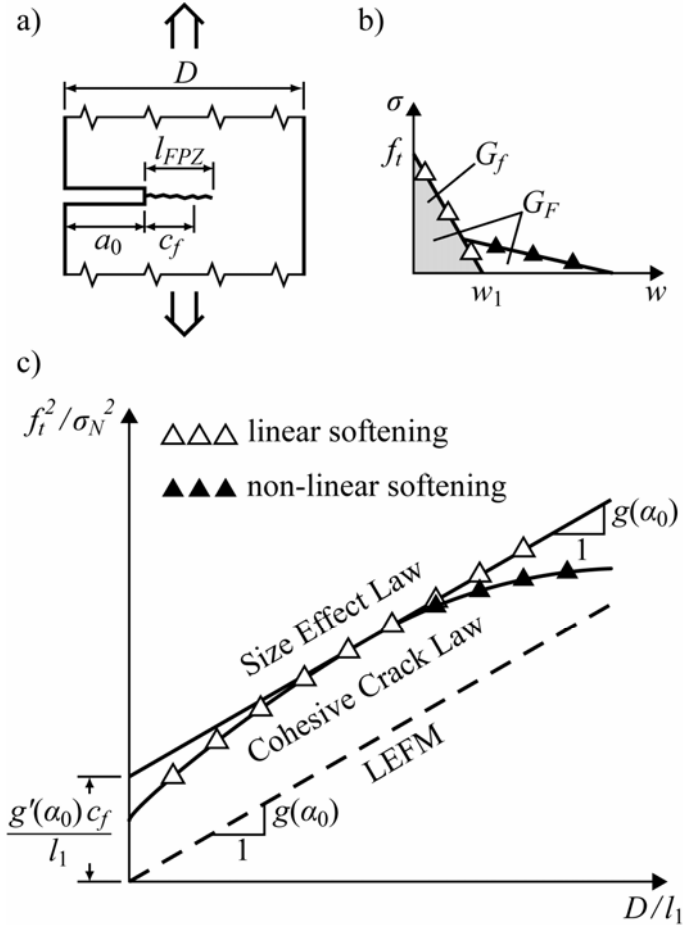


Figure 1. a) Definition of the fracture process zone length and of the crack extension. b) Bi-linear cohesive crack law. c) Size effect law.

The use of the initial fracture energy in the framework of the Equivalent LEFM may seem questionable since this theory implicitly assumes a fully developed FPZ characterized by a vanishing cohesive stress at the tip of the stress-free crack. Indeed, such hypothesis would require the use of the total fracture energy G_F instead of G_f . However, the SEL with G_f coincides with the asymptotic response shown by the cohesive crack model (Bažant 2002) with linear softening, which, in turn, can be used to approximately simulate the response of specimens whose strength is only influenced by the initial part of the softening law (medium size specimens).

In order to exploit the equivalence between the SEL and the asymptotic behavior of the cohesive crack model it is useful to multiply both sides of Equation 1 by the square of f_t (tensile strength), and, introducing the concept of characteristic length $l_1 = EG_f/f_t^2$, to rewrite the SEL as follows

$$\frac{f_t^2}{\sigma_N^2} = g(\alpha_0)\frac{D}{l_1} + g'(\alpha_0)\frac{c_f}{l_1} \quad (2)$$

which represents a straight line in the plane $Y = (f_t/\sigma_N)^2$, $X = D/l_1$ (Fig. 1c).

2.2 Cohesive Crack Law

The propagation of a cohesive crack may be modeled through finite element calculations based on a given $\sigma - w$ relationship. With very accurate mesh layouts in the region of crack propagation it is possible to detect both the maximum load and the extension of the corresponding fracture zone for a given specimen dimension D .

If one assumes a linear expression for the $\sigma - w$ relationship (Fig. 1b, line with white triangles), the resulting nominal stress at failure (structural strength) satisfies a unique relation which can be expressed in the form $\sigma_N = f_t\psi(D/l_1)$, in which the function ψ depends on the geometry of the specimen (Planas, Guinea & Elices 1997) and can be obtained through an optimum fitting of numerical results. We can then define a "Cohesive Crack Size Effect Law" (CCL) in the form

$$\frac{f_t^2}{\sigma_N^2} = \psi^{-2}\left(\frac{D}{l_1}\right) \quad (3)$$

Although, for concrete, linear $\sigma - w$ relationships have been adopted in the past, it appears that a bilinear law with an initial (up to one fifth of the tensile strength) steep slope followed by a tail with mild inclination (Fig. 1b, white and black triangles) can better fit available experimental data.

However, at the peak load the material in the softening regime reaches the tail only for large enough specimens. Consequently, Equation 3 can be used to model the structural strength of small to medium

size specimens (“small”, “medium”, and “large” respect to the characteristic length l_1).

It can be verified that Equation 3 has as a straight line asymptote in the plane $Y = (f_t/\sigma_N)^2$, $X = D/l_1$. Since the SEL is a straight line in the same plane, it is always possible to make the SEL coincide with the CCL asymptote. Furthermore, since the SEL embeds the effect of different specimen shapes and boundary conditions through the dimensionless energy release rate $g(\alpha)$, if the crack extension c_f is proven to be a material property, it is possible to establish a unique relationship between c_f and the parameters of the cohesive law. We will verify in the following that c_f can be considered proportional to the characteristic length l_1 and that the coefficient of proportionality is approximately constant regardless of specimen shape and boundary conditions (a similar result was obtained by Planas & Elices 1993).

In most of the situations, the convergence of the CCL to the asymptote is very fast and so the SEL represents, in a certain range of sizes (Fig. 1c), a very accurate approximation of the CCL (Bažant et al. 2002). In this situation both laws should provide approximately the same initial fracture energy and tensile strength when used to identify those parameters from experimental data relevant to size effect.

In the next sections we will verify this statement and its limitations, and we will quantify the limits of applicability of the linear cohesive law with reference to an extensive experimental and computational effort recently conducted at Politecnico di Milano.

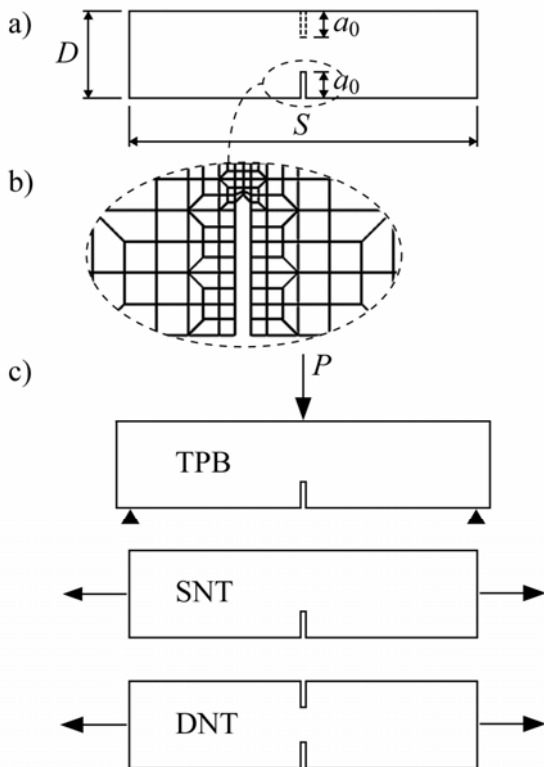


Figure 2. Typical a) notched specimen geometry, b) finite element mesh resolution, and c) boundary conditions considered in the simulations.

2.3 Numerical Simulations

The numerical simulations were performed with a finite element code, in which the cohesive crack law is implemented through the use of zero-thickness interface elements (Carlucci 2003). A great deal of effort was put into the construction of very refined meshes in the region of the crack propagation (Fig. 2b). These meshes were designed in order to give an accurate representation of the stress profile in the FPZ and to accurately calculate the maximum load.

Three kinds of tests were considered: three point bending (TPB), single notch traction (SNT), and double notch traction (DNT) (Fig. 2c). The specimens were rectangular plates (Fig. 2a) having thickness $B = 80$ mm, depth $D = 60, 120, 240, 480, 720, 960, 1440, 1920,$ and 3840 mm, length $S = 4D$, and notch length $a_0 = \alpha_0 D$, with $\alpha_0 = 0.3$. For all sizes, the notch was kept of constant width (3 mm) and constant curvature at the tip. The values adopted for the mechanical properties of the material were $E = 30000$ N/mm², $\nu = 0.2$, $f_t = 3$ N/mm², $G_f = 0.030$ N/mm (linear softening), $l_1 = E G_f / f_t^2 = 100$ mm.

For the TPB specimens, the finite element calculations yielded, for every depth D , the nominal stress at failure $\sigma_N = 3P_{\max}S/(2BD^2)$ and the stress distribution along the ligament (Fig. 3a), from which the length of the fracture process zone l_{FPZ} and the tensile stress at the tip of the notch σ_{tip} (Fig. 3c and 3d, respectively) could be determined.

The plot of $Y = (f_t/\sigma_N)^2$ as a function of $X = D/l_1$, reported in Figure 3b, shows the presence of an asymptote $Y = AX + C$, with $A = 1.021$ and $C = 2.036$. The slope of the asymptote (obtained by passing a straight line through the last two points of the diagram) has a value (1.021) which practically coincides with the value of $g(\alpha_0) = 1.0247$ reported by Tada et al. (1985) for TPB specimens. This confirms that the SEL and the CCL asymptote have the same slope. It has been checked that the slope of the line which connects the last two points of the CCL data points differs from the actual slope of the asymptote by less than 1%.

The length l_{FPZ} of the fracture process zone increases with D/l_1 , as shown in Figure 3c, reaching a horizontal asymptote given by $l_{FPZ,\infty} = 68$ mm ($l_{FPZ,\infty} = 67.96$ mm for $D = 3840$ mm). In addition, it is also possible to calculate the crack extension c_f from the intercept $C = 2.036$ of the asymptote: $c_f = CE G_f / g'(\alpha_0) = 38.8$ mm.

The stress at the notch tip decreases with D/l_1 , reaching a value of $\sigma_{tip}/f_t = 0.05$ for $D = 3820$ mm. However, from Figure 3d it appears that the linear σ - w relationship ceases to be valid for values of D/l_1 of around 5.8 for which $\sigma_{tip}/f_t = 0.2$. A bilinear σ - w relationship would increase the value of l_{FPZ} , change the shape of the stress distribution in the FPZ (Fig. 3a), and make the curve $(f_t/\sigma_N)^2$ deviate from the asymptote for high values of D/l_1 , as shown in Figure 1c.

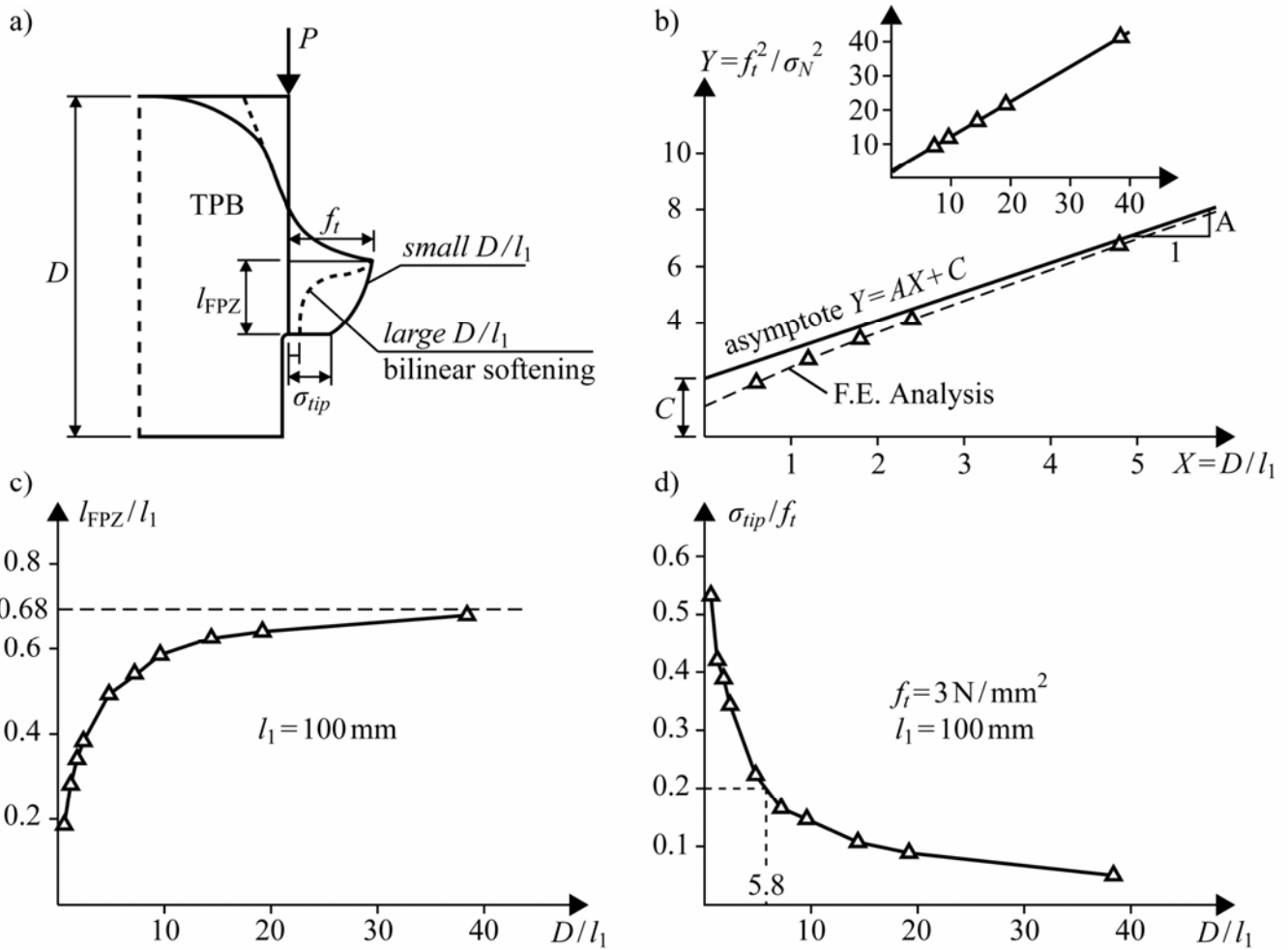


Figure 3 a) Typical stress profile in the FPZ. b) CCL size effect curve and its asymptote. c) Normalized FPZ length. d) Normalized crack tip stress at the peak load.

The numerical calculations have been repeated for single and double-notched traction specimens of the same dimensions. Table 1 (Auriemma & Avogadri 2005) summarizes the results obtained for the three types of loading.

Table 1a

	A	C	$g(a_0)$	$g'(a_0)$
TPB	1.021	2.036	1.024	5.246
SNT	2.602	8.020	2.590	19.64
DNT	1.184	1.469	1.190	3.988

Table 1b

	$l_{FPZ,\infty}$ mm	$l_{FPZ,\infty}/l_1$	c_f mm	c_f/l_1	$c_f/l_{FPZ,\infty}$
TPB	68	0.68	38.8	0.388	0.57
SNT	70	0.70	40.7	0.407	0.58
DNT	71	0.71	36.8	0.368	0.52

From Table 1 it appears that there is a consistent agreement between the predictions of the CCL (with linear softening) and the SEL. The length of the fracture process zone approaches a value $l_{FPZ,\infty}$ which is practically independent of the loading type and can therefore be regarded as a material property, as is the case for the equivalent crack extension c_f .

The ratio between the crack extension c_f and the asymptotic length of the fracture process zone $l_{FPZ,\infty}$

is very close to the value (0.5) proposed by Bažant & Planas (1998).

Table 1b shows also that $c_f/l_1 = 0.39$ is a good approximation for all three types of loading (Bažant & Planas 1998, reported 0.42). The previous observation confirms that a unique relationship between the SEL parameters (G_f , c_f) and the cohesive crack parameters (G_f , f_t) can be then assumed. In particular, it is possible to compute the tensile strength from the SEL parameters $f_t = (0.39 E G_f / c_f)^{1/2}$. In the authors' knowledge, this is the first time that this procedure to identify f_t has been analyzed.

3 TESTING OF FRACTURE PARAMETERS

A series of experimental investigations have been conducted at the Politecnico di Milano with the purpose of determining the fracture characteristics related to the initial part of the $\sigma - w$ curve, i.e. the part of the curve which can be modeled with a linear relationship, the parameters of which are f_t and G_f . For different concrete compositions, besides three point bending specimens, also traction and Brazilian specimens were tested. We will report here the test results relative to the TPB specimens, in order to analyze the predictions of the SEL and CCL and evaluate their statistical reliability.

The characteristics of the four concrete batches are summarized in Table 2.

Table 2

	Aggregate		Cement		w/c	E	f _c
	Type	d _a mm	Portland	Quantity kg/m ³			
N	A	16	325	300	0.60	24200	28.5
S	F	16	325	570	0.44	28600	54.8
B	A	16	325	330	0.55	32680	33.7
C	A	16	325	380	0.50	28690	49.6

3.1 Three Point Bending Tests

3.1.1 Concrete "N"

The specimens tested (Fig. 2a) are characterized by a ratio $S/D = 8/3$, $\alpha_0 = 0.3$, notch width 3 mm, depth $D = 120, 180, 240$ mm and thickness $B = 80$ mm. The loading rate adopted is $\dot{\sigma}_N = 0.012 \text{ N mm}^{-2} \text{ sec}^{-1}$. For each size, a series of three specimens was tested. The mean values of σ_N at failure are reported in Table 3 (Taini 2002), together with their coefficient of variation ω .

Table 3

D mm	σ_N N/mm ²	ω %
120	2.07	6.15
180	1.77	7.53
240	1.62	3.35

The identification of the SEL parameters from the mean values in Table 3 can be done through a linear regression line (Eq. 1a) $y = ax + c$, in which $y = 1/\sigma_N^2$ and $x = D$, obtaining $a = 0.001228$, $c = 0.09020$, from which $G_f^{\text{SEL}} = g(\alpha_0)/Ea = 0.0345 \text{ N/mm}$ and $c_f^{\text{SEL}} = cEG_f^{\text{SEL}}/g'(\alpha_0) = 14.35 \text{ mm}$, $f_t^{\text{SEL}} = (0.39 EG_f^{\text{SEL}}/c_f^{\text{SEL}})^{1/2} = 4.76 \text{ N/mm}^2$, and $l_1^{\text{SEL}} = 36.78 \text{ mm}$.

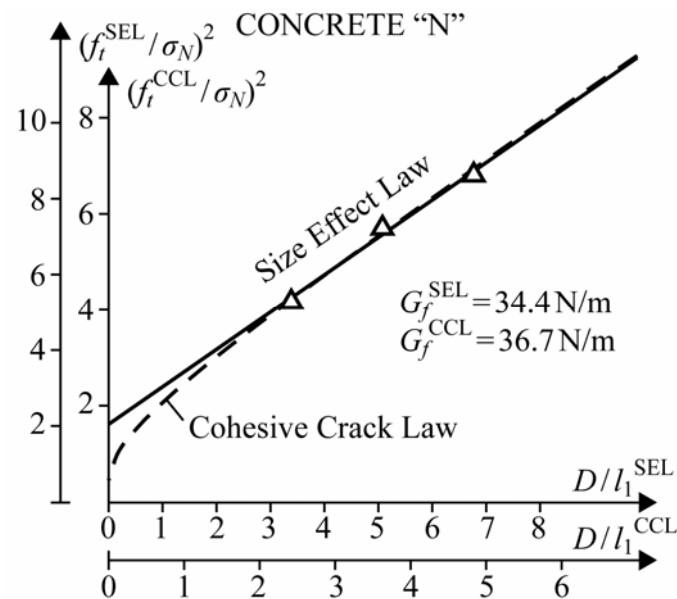


Figure 4. Identified SEL and CCL for concrete "N".

The identified SEL is plotted in Figure 4.

Let us analyze now the same results through the cohesive crack model (with linear softening), adopting as function ψ the expression proposed by Planas et al. (1997) for three point bending specimens (calculated for the given value of α_0)

$$\psi = \frac{\sigma_N}{f_t} = 1.47 \left[\frac{1 + 3.843\sqrt{z}}{1 + 0.5651\sqrt{z}} + 2.2288z \right]^{-1/2} \quad (4)$$

where $z = D / l_1^{\text{CCL}}$.

Each experimental mean value of σ_N gives rise in the (f_t, G_f) plane to a different curve (Fig. 5b). By minimizing the sum of the squares of the errors in fitting Equation 4, one obtains the values $f_t^{\text{CCL}} = 4.23 \text{ N/mm}^2$, $G_f^{\text{CCL}} = 0.0367 \text{ N/mm}$. Figure 5a shows the estimated errors in σ_N with respect to the model in Equation 4, and Figure 5c shows the curves corresponding to the σ_N values predicted by the model. The observation that the interceptions of the various curves occur with slopes which are very close indicates (as pointed out by Planas et al. 1999) that the identification process may be, in principle, ill-conditioned and thus very sensitive to the unavoidable statistical scatter of the experimental data.

The CCL size effect curve is shown in Figure 4 as a dashed line. Its asymptote differs only slightly from the SEL. The results of the analysis of concrete "N" are summarized in Table 4.

The agreement between the SEL-scale and the CCL-scale in Figure 4 suggests that the two optimization procedures are basically equivalent. The difference between the identified values of the initial fracture energy and tensile strength is about 6% and 13%, respectively.

The smallest experimental ratio D/l_1 is larger than 2.5 and so the difference between SEL and CCL is very small. The largest experimental ratio D/l_1 lies between 5.14 and 6.5. As a consequence, the stress at the notch tip could be slightly smaller than the limit of $f_t/5$ (for which $D/l_1=5.8$) justifying the slight deviation from the linearity of the third experimental data point.

Table 4

	G _f N/mm	c _f mm	f _t N/mm ²	l ₁ mm
SEL	0.0345	14.35	4.76	36.78
CCL	0.0367	18.18	4.23	46.63

The obtained values for the crack extension c_f (14.35 mm from the SEL and 18.18 mm from the CCL) are of the order of magnitude of the maximum aggregate size. At first sight, this result seems quite unusual and counterintuitive since c_f is associated to the size of the fracture process zone. A possible in-

terpretation of this result can stem from the meso-scale analysis of the fracture process.

In section 5, by using a two-scale procedure and a meso-scale lattice model, it will be demonstrated that the initial fracture energy basically coincides with the meso-level mode I fracture energy. In the aforementioned lattice model (see e.g. Cusatis et al 2003a), the mesolevel fracture energy is used to reproduce the dissipation phenomena that occur in the matrix (cement paste and/or fine mortar) between coarse aggregate pieces. These phenomena (and so the meso-level fracture energy) are necessarily associated with a meso-scale fracture process zone whose size can be reasonably assumed of the order of magnitude of the maximum aggregate size. As a consequence, it is reasonable to consider the crack extension c_f associated with this meso-scale FPZ instead of the macro-scale FPZ, whose size is expected to be several times the maximum aggregate size.

We have based the previous analysis on the mean values of the test results for each dimension D . In order to assess the variability of the experimental values of σ_N (typically three for each D) and the statistical reliability of the parameters obtained with the optimization procedure, we performed “bootstrap” resampling (Efron and Tibshirani 1993) of the original sets of test results. One thousand resampled data sets were generated by drawing with replacement from the sets of σ_N (typically three) measured for each dimension D . Values of σ_N corresponding to different D were drawn independently from each

other. The mean of the resampled values of σ_N corresponding to each D was used in the optimization, which was repeated for each of the 1000 bootstrap resamplings of the data. This procedure allowed us to quantify the relationship between the typical variation in the experimental measures of σ_N and the resulting variations of the optimized parameters f_i and G_f , without making any assumption about the underlying distributions.

Due to the asymmetrical shape of the observed distributions of the optimized parameters (Fig. 6a,b), we chose to report the median, the 15th percentile and the 85th percentile of each distribution, instead of the mean and standard deviation (the 15th percentile and the 85th percentile define an interval, positioned around the median, capturing 70% of the observed outcomes of the optimized parameters – analogous to mean \pm standard deviation for a normal distribution).

The value of the medians, $G_f^m = 0.0364$ N/mm and $f_i^m = 4.2673$ N/mm², were very similar to the values obtained with the original set of data (we will see that this happens for all concretes). However, the values of the 15th and 85th percentiles showed large percentage deviations relative to the medians ($G_f^{15} = 0.029$ N/mm (-21%), $G_f^{85} = 0.050$ N/mm (+37%), $f_i^{15} = 3.057$ N/mm² (-28%), $f_i^{85} = 7.152$ N/mm² (+68%)), indicating poor precision associated to estimating G_f and f_i using the CCL for this type of concrete.

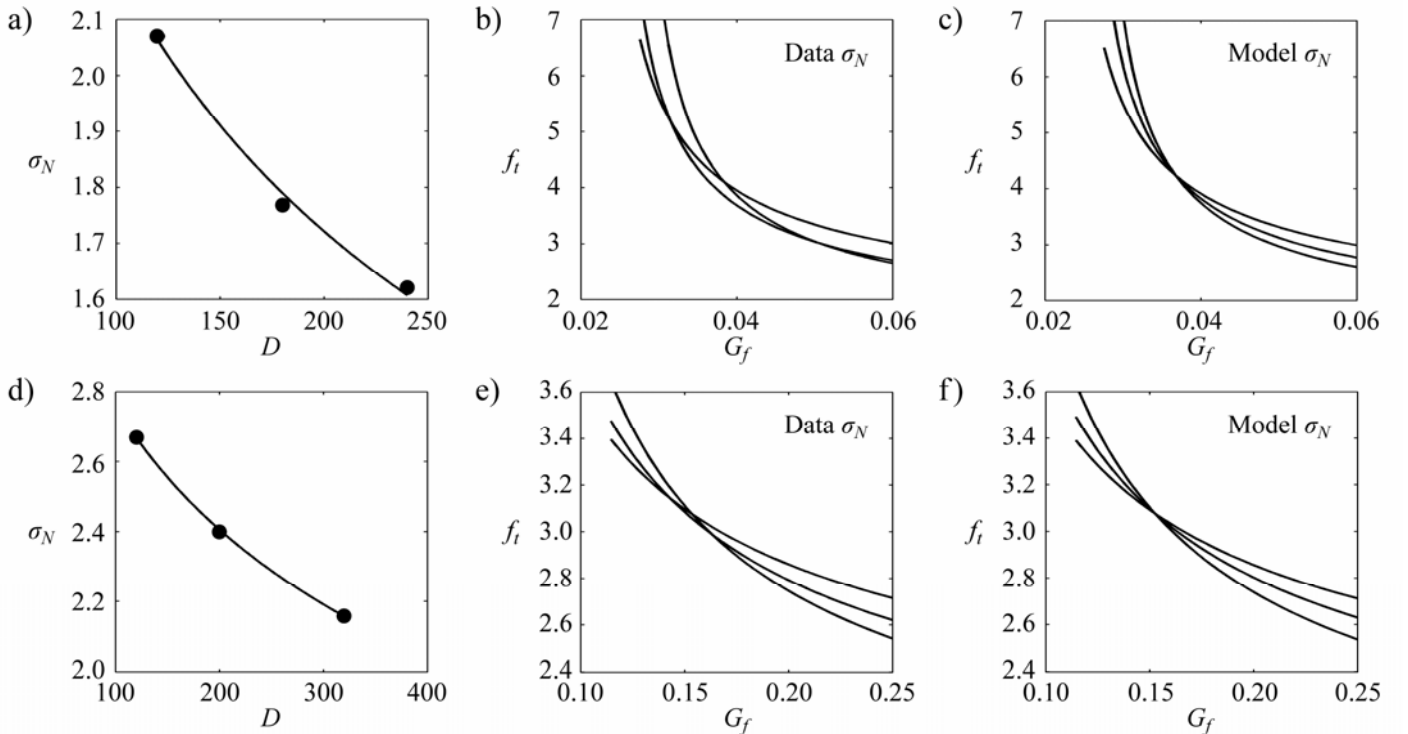


Figure 5. a,d) Experimental data (circles) and CCL-based least-squares fits (lines) for concretes “N” (a) and “C” (d). b,e) $f_i - G_f$ curves based on experimental pairs (D, σ_N) for concretes “N” (b) and “C” (e). c,f) Same as in b,e, but using values of σ_N predicted by the model.

We repeated the procedure for the SEL, calculating for each bootstrap resampling the parameters G_f and c_f predicted by the SEL and examining their distributions (Fig. 6c,d). Again the medians $G_f^m = 0.0345$ N/mm and $c_f^m = 14.414$ mm matched very closely to the values obtained directly from the original set of data. For the SEL, however, the 15th and 85th percentiles ($G_f^{15} = 0.0301$ N/mm (-13%), $G_f^{85} = 0.0409$ N/mm (+19%)) indicate a somewhat smaller variability for G_f with respect to the CCL. The values ($c_f^{15} = 7.66$ mm (-47%), $c_f^{85} = 23.88$ mm (+66%)) show a similar dispersion for c_f compared with the parameter f_i of the CCL.

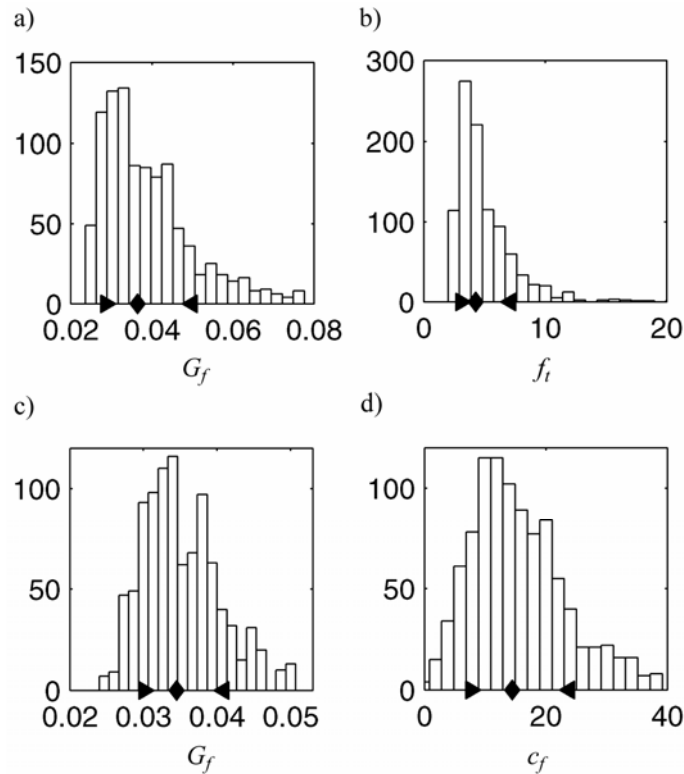


Figure 6. Concrete “N”: histograms of the distributions of the optimized parameters across 1000 bootstrap resamplings of the original data sets. a,b) CCL; c,d) SEL. Diamonds: median values. Triangles: 15th and 85th percentiles.

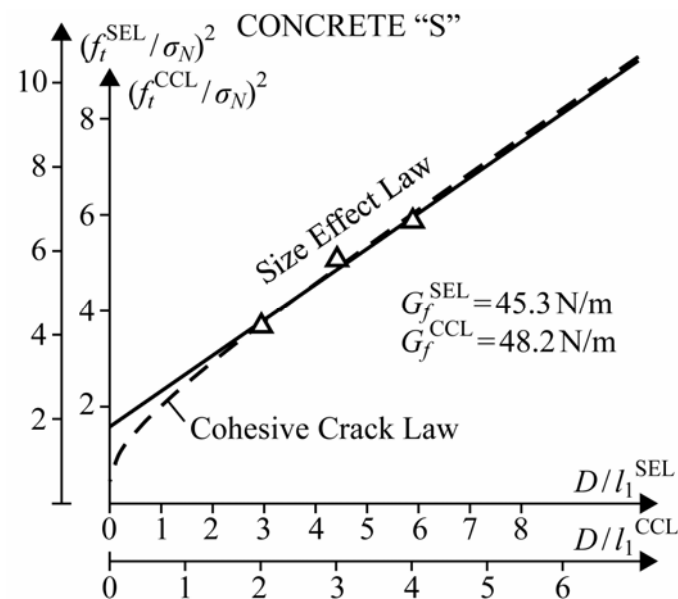


Figure 7. Identified SEL and CCL for concrete “N”.

3.1.2 Concrete “S”

The geometry and the number (3) of the specimens is the same as in concrete “N”. The mean values of the nominal stress σ_N at failure and their coefficient of variation ω are listed in Table 5 (Taini 2002).

Table 5

D mm	σ_N N/mm ²	ω %
120	2.50	2.46
180	2.13	2.84
240	1.98	4.75

Table 6

	G_f N/mm	c_f mm	f_i N/mm ²	l_1 mm
SEL	0.0453	16.99	5.20	43.57
CCL	0.0482	21.95	4.78	56.30

For the SEL, the linear regression line has parameters $a = 0.00079$ and $c = 0.06874$, which lead to the values summarized in the first row of Table 6. Instead, the second row of Table 6 shows the results obtained through the nonlinear optimization of Equation 4. Figure 7 shows that the asymptote of the CCL curve differs very slightly from the SEL.

These results appear very similar to those obtained for concrete “N” and so the same conclusions can be drawn.

The median values of the optimized parameters (CCL) obtained from bootstrapping were $G_f^m = 0.0482$ N/mm and $f_i^m = 4.787$ N/mm². The percentage deviations from the median of the 15th and 85th percentiles were (-16%, +26%) for G_f and of (-18%, +25%) for f_i , smaller values than those obtained for concrete “N”. The SEL gave median values of $G_f^m = 0.0452$ N/mm, $c_f^m = 16.76$ mm, with deviations of (-15%, +19%) for G_f and of (-41%, +52%) for c_f , slightly smaller than for concrete “N”, but still unsatisfactory. The distributions appear more symmetric than those for concrete “N” (not shown).

3.1.3 Concrete “B”

Also for concrete “B” the geometry and the number (3) is the same as in concrete “N”. The mean values of the nominal stress at failure are reported in Table 7 (Barcillesi and Baroni 2003).

Table 7

D mm	σ_N N/mm ²	ω %
120	2.69	1.84
180	2.38	1.28
240	2.22	3.56

The parameters of the linear regression line for the fitting of the SEL have values $a = 0.0005336$ and

$c = 0.07634$, with the parameters summarized in the first row of Table 8. The optimization of the CCL (Eq. 4) produces, instead, the parameters reported in the second row of Table 8.

In this case the agreement between the SEL and the CCL is very poor. The differences between the identified initial fracture energy and tensile strength with the two methods are about 18% and 30%, respectively. The crack extensions and the characteristic lengths computed through the two methods differ of almost 100%. The reason of this discrepancy is clearly shown by Figure 8: the SEL does not coincide with the asymptote of the CCL because the experimental ratios D/l_1 lie in the range of values for which the CCL curve deviates significantly from the CCL asymptote.

Table 8

	G_f N/mm	c_f mm	f_t N/mm ²	l_1 mm
SEL	0.0588	27.94	5.18	71.65
CCL	0.0719	47.52	3.97	121.84

The median values of the optimized parameters (CCL) obtained from bootstrapping were $G_f^m = 0.0740$ N/mm and $f_t^m = 3.9135$ N/mm². The percentage deviations from the median of the 15th and 85th percentiles were (-16%, +22%) for G_f and (-10%, +12%) for f_t . The SEL yielded median values of $G_f^m = 0.059$ N/mm and $c_f^m = 28.284$ mm, with deviations of (-11%, +13%) for G_f and of (-23%, +26%) for c_f . Overall, the distributions are more symmetric and the dispersion is smaller compared to concretes "N" and "S".

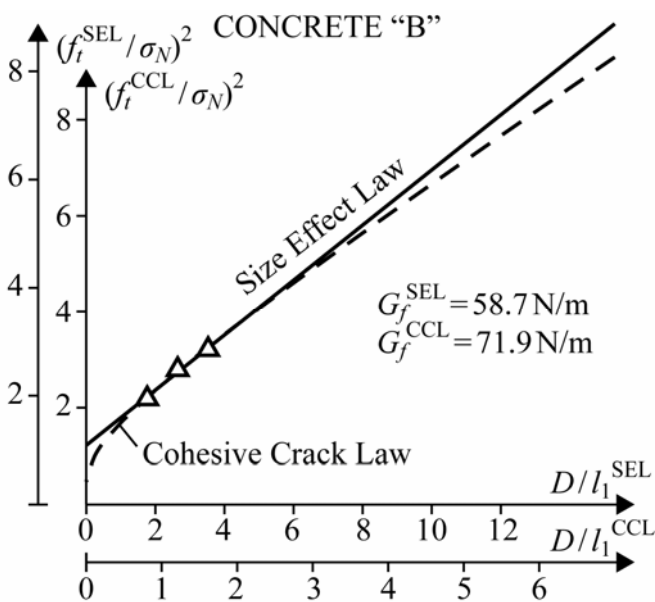


Figure 8. Identified SEL and CCL for concrete "B".

3.1.4 Concrete "C"

The geometry of the specimens remained unchanged for concrete "C", except for the depths ($D = 120, 200, \text{ and } 320$ mm) and the number of specimens (four for each depth D). The mean values of σ_N at failure are listed in Table 9 (Colombo 2004) together with their coefficient of variation.

Table 9

D mm	σ_N N/mm ²	ω %
120	2.67	4.47
200	2.40	3.86
320	2.16	5.56

Table 10

	G_f N/mm	c_f mm	f_t N/mm ²	l_1 mm
SEL	0.0986	53.27	4.55	136
CCL	0.1526	117	3.07	300

The parameters of the linear regression line are $a = 0.000362$ and $c = 0.09875$, from which the parameters appearing in Table 10 (first row) can be obtained. The second row of Table 10 shows, instead, the parameters identified through the CCL. Again, as in the case of the concrete "B" the difference between the parameters identified through the two methods is very large. The difference in terms of initial fracture energy and tensile strength is 35% and 48%. The characteristic length associated with the CCL is more than twice the one associated with the SEL. Similarly to the case of concrete "B" the reason of this discrepancy is that the experimental ratios D/l_1 lie in a range in which the CCL curve deviates from the CCL asymptote (see Fig. 9).

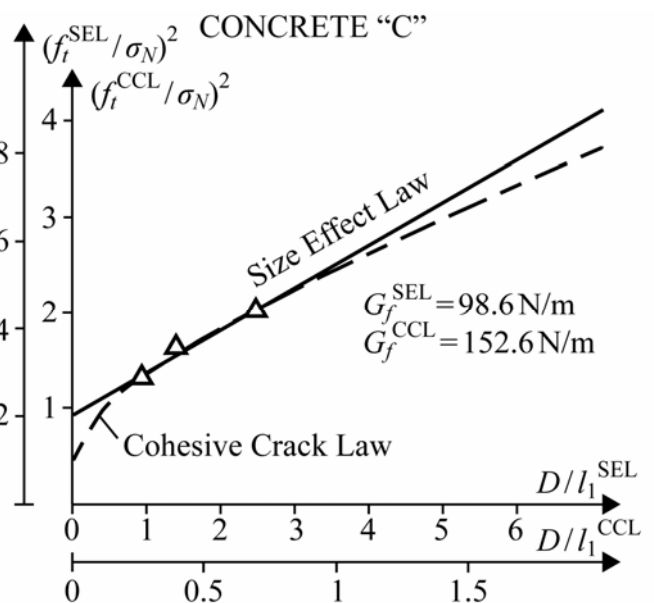


Figure 9. Identified SEL and CCL for concrete "C".

It is interesting to point out that in this case the experimental results are particularly close to the predictions of the cohesive crack law, as demonstrated by Figures 5d,e and f.

The median values of the optimized parameters (CCL) obtained from bootstrapping were $G_f^m = 0.1566$ N/mm and $f_t^m = 3.0539$ N/mm². The percentage deviations from the median of the 15th and 85th percentiles were (-28%, +49%) for G_f and (-12%, +14%) for f_t . The SEL yielded median values of $G_f^m = 0.0991$ N/mm and $c_f^m = 53.94$ mm, with deviations of (-18%, +25%) for G_f and of (-30%, +39%) for c_f .

4 DIRECT MEASUREMENT OF STRESS SEPARATION RELATION

We have seen that the process of identifying the parameters of the cohesive crack law from overall measurements of the maximum load is affected by a significant statistical uncertainty. Also, more direct methods which involve strain gage measurements on specimens under a pure tensile loading encounter technical and interpretative difficulties. A more accurate picture can be obtained from local measurements of the displacement field through optical interferometry with laser light (Cedolin, Dei Poli and Iori 1987), carried out by analyzing the moiré fringe pattern produced by a grid photographically impressed on the specimen surface. With this technique the distances of the fringes give a measure of the deformation, while the number of superimposed fringes indicates the value of the crack opening.

The specimen used was a single notched plate under tension. The contours of equal deformation at a loading state close to failure, depicted in Figure 10a, clearly indicate the extension of the fracture process zone, the lower part of which is close to a complete unloading. The strain distribution along the cross sections E-E and D-D are shown in Figure 10b,c, together with the crack opening displacement (lower part of Fig. 10c). From the observed strain and separation distributions corresponding to different loading stages, the parameters σ , η and η_R (Fig. 11) of the local stress-strain and stress-separation relationships were identified. The values obtained for the fracture energies $G_f' = 0.004$ N/mm due to microcracking and $G_f'' = 0.070$ N/mm due to crack separation confirm the validity of the original Hillerborg's assumption of incorporating G_f' into G_f'' . The value of the maximum tensile stress $\sigma = 4.0$ N/mm² was larger than the tensile strength measured from tensile tests (3.1 N/mm²) and the maximum measured crack opening was $\eta = 35$ μ m.

We introduced the constitutive law so obtained in the cohesive crack finite element model previously described, finding a maximum axial load of 9258 N, astonishingly close to the measured 9244 N. The contours of equal deformations and the distributions

of strain and opening displacement along the cross sections E-E and D-D (Fig. 10d,e,f) appear very similar to the experimental ones.

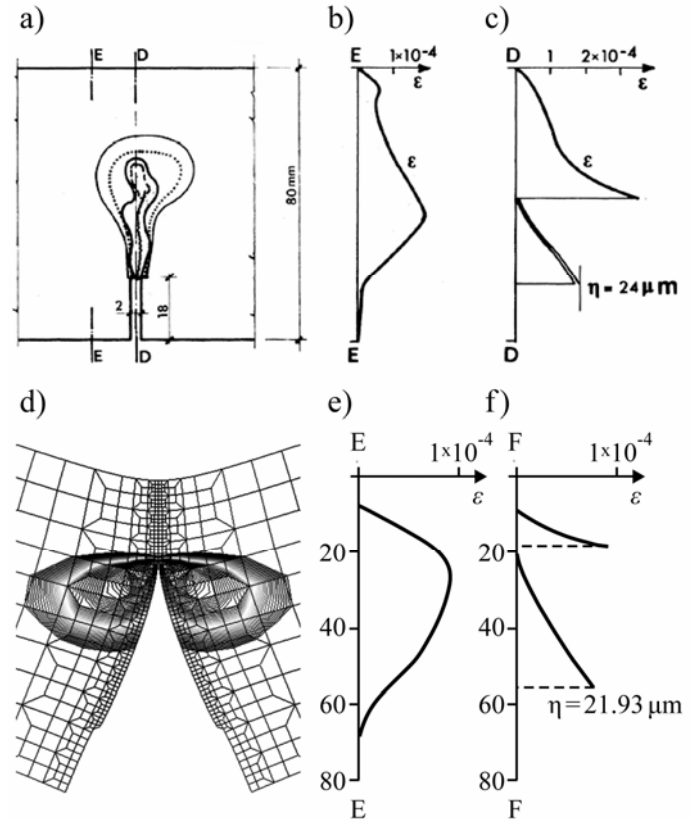


Figure 10. a) Equal strain contours and developing crack. b,c) Strain distributions and crack opening profile. d,e,f) Equal strain contours, strain distributions and crack opening profile from finite element analysis.

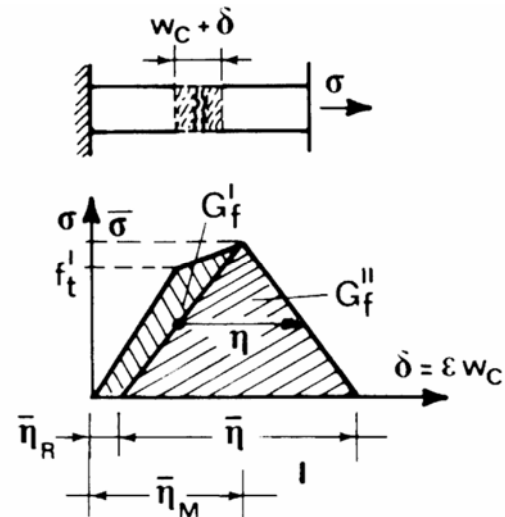


Figure 11. Stress - crack opening displacement relationship identified in Cedolin, Dei Poli & Iori (1987).

5 MESOLEVEL MODELING OF FRACTURE

In this section typical experimental procedures used for the characterization of the fracturing behavior of concrete, namely single notched specimens subjected to tensile loading and three-point bending, are analyzed on the basis of the Confinement-Shear Lattice (CSL) model, which is a mesolevel model re-

cently developed by the authors (Cusatis et al 2003a, Cusatis et al 2003b, Cusatis et al 2006, Cusatis & Cedolin 2006). Through a two-scale procedure an equivalent macroscopic cohesive crack law is obtained from the meso-level response in order check the variability of the fracturing properties of concrete with specimen size and loading conditions.

5.1 Two-scale Identification of the Cohesive Law

Previous studies (e.g. Cusatis et al 2006) have demonstrated that the CSL model is able to simulate accurately the propagation of mode I and mixed mode fracture propagation in concrete. Figure 1a shows a typical simulation of a mode I fracture propagating from the tip of a preexisting notch.

The fracture initiates at the notch tip and propagates throughout the ligament. The analysis of the numerical response shows that the fracture process is characterized by the propagation of a system of mesolevel cracks (contact areas of the lattice elements) that eventually coalesce in a single localized crack. Accordingly, in the initial stage of the fracture process the energy is dissipated in a band of finite width (crack band). This behavior is well known experimentally and it has motivated the formulation of the crack band model (Bažant & Oh 1983).

The aim of the present analysis is the identification of an equivalent cohesive crack that lumps the behavior of the FPZ in a zero thickness cohesive fracture running along the ligament. This goal can be achieved by adopting the following procedure. The specimen is subdivided into stripes parallel to the direction of the applied load. These stripes discretize the ligament into segments of length h (Fig. 12b). For each ligament segment it is possible to compute the dissipated energy per unit ligament area g_d that would be dissipated by the propagation of an equivalent cohesive macro-crack, and the cohesive stress σ_{ch} . The energy g_d is computed by summing up the contributions of the fractured lattice elements belonging to a generic stripe. The cohesive stress is calculated from the components in the direction of the applied load of the lattice forces crossing the ligament. Furthermore, the macro-crack opening displacement w (opening profile of the equivalent cohesive crack) can be calculated by observing that it represents the work-conjugate kinematic quantity of the cohesive stress. Thus, the increment of the dissipated energy is the work done by the cohesive stress for an increment of the crack opening, $dg_d = \sigma_{ch} dw$. This differential equation can be solved for w under the initial condition $w(0) = 0$ in order to obtain the function $w(g_d)$ that gives the crack opening as function of the dissipated energy. By repeating the preceding procedure for each loading step we obtain a parametric representation of the equivalent cohesive crack law, $\sigma_{ch}(g_d) - w(g_d)$, at each discrete point

along the ligament. In Cusatis & Cedolin (2006) it has been shown that an optimum fit of these numerical cohesive crack laws can be obtained by assuming a cohesive crack law with an initial plateau followed by a smooth curve consisting of the sum of a straight line and an exponential function.

The initial plateau simulates the energy dissipated in the FPZ before the propagation of a real macro-crack. From a rigorous point of view, this energy should be taken into account by assuming a plastic hardening behavior of the stress-strain relationship of the intact concrete (Fig. 11 from Cedolin et al. 1987). Nevertheless, this approximation is reasonable because the amount of this energy is usually negligible compared to the energy dissipated during the entire fracture process. Regarding the tail of the identified softening curve, it is worth pointing out that the linear evolution is due to the effect of the aggregates bridging the crack surfaces and it does not depend on the constitutive law at the mesolevel, which is purely exponential (Cusatis et al 2003a). Once the cohesive law is identified, it is also possible to calculate the initial and total fracture energy (G_f and G_F in Figure 1b).

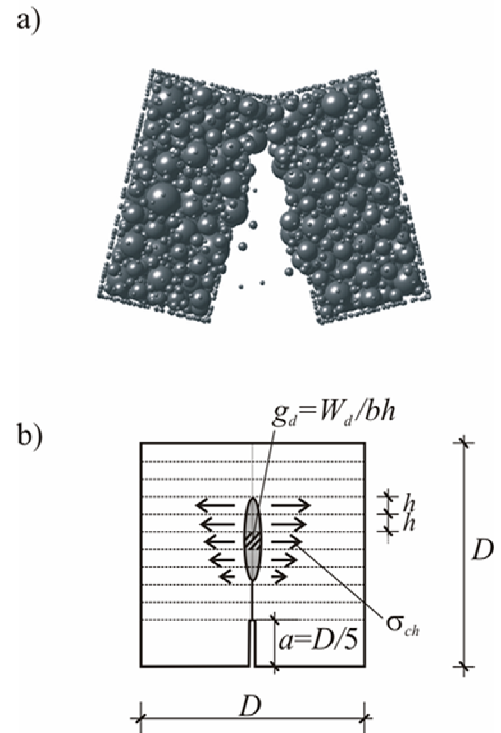


Figure 12. a) Typical result of a mesolevel simulation of mode I fracture propagation. b) Identification of cohesive stresses and dissipated energy per unit ligament area.

5.2 Size and Boundary Condition Dependence of The Fracture Energies

Experimental data available in the literature (e.g. Hu & Wittmann 1992) show that the total fracture energy depends on specimen size and boundary conditions. In order to study these effects the previous

identification procedure has been repeated for two sets of geometrically similar specimens.

The first set consists of square notched specimens of side D and notch $a = D/5$, subjected to tension under displacement control (SN test). The second set is composed by rectangular notched plates of depth D , length equal to $2.5D$, and notch equal to $D/5$, loaded in displacement control by a three point bending test setup (TPB test). In the numerical simulations of the TPB tests only the central part of the specimen is modeled by means of the lattice model while conventional finite elements are employed for the lateral parts where the behavior is expected to be linear elastic.

For both sets the simulation of specimens with characteristic size equal to $D = 100$ mm (small, S), $D = 200$ mm (medium, M), and $D = 300$ mm (large, L) has been carried out. Three specimens with different mesostructure are analyzed for each size. All the specimens had thickness $b = 50$ mm.

The results obtained by the SN test are shown in Figure 13a where the identified values of the initial and total fracture energy are plotted as functions of the position along the ligament. In order to compare results for different sizes the dimensionless coordinate x/D is employed.

The initial fracture energy G_f is constant over the entire ligament, and, regardless the size of the specimen (Cusatis & Cedolin 2006) it basically coincides with the mesolevel fracture energy for mode I crack propagation.

On the contrary, the total fracture energy G_F varies along the ligament and it is size dependent. For each specimen size, the total fracture energy tends first to increase, moving from the notch tip to the interior of the specimen, and then to decrease while it propagates towards the opposite boundary. This result suggests that the asymptotic length of the FPZ (l_{FPZ}), which is the length of a fully developed FPZ characterized by a stress profile varying from the tensile strength to zero, is larger than the specimen ligament even for the largest specimen. This fact can be further verified by estimating l_{FPZ} by means of the equivalent linear elastic fracture mechanics (Bažant & Planas 1998). For the concrete properties analyzed in this paper Cusatis & Cedolin (2006) have estimated l_{FPZ} between 1.14 m and 2.85 m. This means that l_{FPZ} is one order of magnitude larger than the ligament of the largest specimen, confirming the impossibility of obtaining a fully developed FPZ in specimens of laboratory size.

As far as the effect of the size is concerned, the results that the mean value of total fracture energy along the ligament increases with the size of the specimen. This finding is in agreement with the experimental data reported by Hu & Wittmann (1992). Figure 13b show the profiles of fracture energies identified by the TPB tests. These results indicate that, also for the TPB tests, the initial fracture energy

is constant along the ligament (with values equal to the ones identified from the SNT test) and size independent. On the contrary, the total fracture energy varies along the ligament and with the size of the specimen. Furthermore, comparing the G_F -profiles obtained from the two different test setups but for the same characteristic specimen size, one can see that the total fracture energy also depends considerably on the type of boundary conditions. The value of G_F identified from the SN test is, on average, larger than the one from the TPB test because in the latter the evolution of the FPZ is more hampered by the compressed part of the ligament.

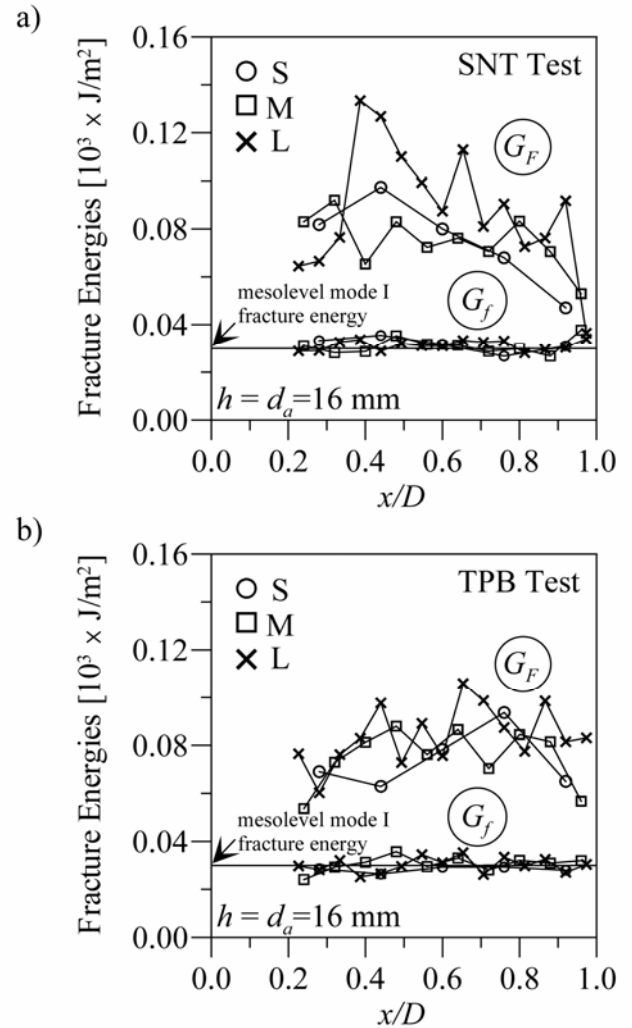


Figure 13. Profiles along the ligament of initial and total fracture energy for a) SN test, and b) TPB test.

6 CONCLUSIONS

From the analysis of the experimental and computational results reviewed in this paper the following conclusion can be drawn:

- 1) The classical Bažant's size effect law is equivalent to the asymptotic behavior given, for large sizes, by the cohesive crack model.

2) Exploiting this equivalence it is possible to establish a unique relationship between the SEL parameters and the cohesive crack law parameters.

3) This relationship permits the identification of the initial fracture energy and the tensile strength from the SEL parameters provided that the SEL is optimized on the basis of specimens whose values of D/l_1 lie in the range 3 to 6, at least for TPB tests with shape similar to the ones considered in this study.

4) For values of D/l_1 less than 3 the errors associated with the use of the SEL, especially in terms of tensile strength, are unacceptable and the CCL must be used.

5) For values of D/l_1 greater than 6 both methods cannot be used.

6) Although the precision of the estimates of the fracture parameters obtained with both methods is low, the initial fracture energy is more reliably estimated using the SEL (within the range of its applicability).

7) The basic assumptions of the cohesive crack model are confirmed by the direct observation of the displacement field at the fracture front.

8) The initial fracture energy is strictly connected to the mesolevel mode I fracture energy.

9) Its identification can be performed by analyzing laboratory specimens.

10) The total fracture energy identified from laboratory specimens strongly depends on specimen size and boundary conditions.

REFERENCES

- Auriemma, M. & Avogadri, M. 2005. Sui Metodi di Misura delle Caratteristiche di Frattura del Calcestruzzo. Master Thesis, Politecnico di Milano.
- Barcillesi, A. & Baroni, S. 2003. Determinazione Sperimentale delle Caratteristiche di Frattura del Calcestruzzo. Master Thesis, Politecnico di Milano.
- Bazant, Z.P. 1984. Size Effect in Blunt Fracture: Concrete, Rock, Metal. *ASCE, Journal of Engineering Mechanics* 110: 518-535.
- Bazant, Z.P. 2002. Concrete Fractures Models: Testing and Practice. *Engineering Fracture Mechanics* 69: 165-205.
- Bazant, Z.P. & Oh, B.H. 1983. Crack Band Theory for Fracture of Concrete. *Materiaux et Constructions* 16: 155-77.
- Bazant, Z.P. & Planas, J. 1998. Fracture and Size Effect in Concrete and Other Quasibrittle Materials. CRC Press, Boca Raton and London.
- Bazant, Z.P., Yu, Q. & Zi, G. 2002. Choice of standard fracture test for concrete and its statistical evaluation. *Int. J. Fracture* 118: 303-337.
- Carlucci, A. 2003. Interazione tra Comportamento Fratturante del Calcestruzzo e Aderenza Acciaio-Calcestruzzo nelle Strutture in C.A.. Master Thesis, Politecnico di Milano.
- Cedolin, L., Dei Poli, S. & Iori, I. 1987. Tensile behavior of concrete. *ASCE, Journal of Engineering Mechanics* 113(3): 431-449.
- Colombo, L. 2004. Analisi di Prove di Frattura sulla Base del Modello Coesivo. Master Thesis, Politecnico di Milano.
- Cusatis, G., Bazant, Z.P. & Cedolin, L. 2003a. Confinement-Shear Lattice Model for Concrete Damage in Tension and Compression. I: Theory. *ASCE, Journal of Engineering Mechanics* 129(12): 1439-1448.
- Cusatis, G., Bazant, Z.P. & Cedolin, L. 2003b. Confinement-Shear Lattice Model for Concrete Damage in Tension and Compression. II: Numerical implementation and Validation. *ASCE, Journal of Engineering. Mechanics* 129(12): 1449-1458.
- Cusatis, G., Bazant, Z.P. & Cedolin, L. 2006. Confinement-Shear Lattice CSL Model for Fracture Propagation in Concrete. Invited paper for the special issue of CMAME entitled *Computational Modeling of Concrete*: 7154-7171.
- Cusatis, G. & Cedolin, L. 2006. Two-scale Analysis of Concrete Fracturing Behavior. Invited paper for the special issue of *Engineering Fracture Mechanics* 74: 3-17.
- Efron, B. & Tibshirani, R.J. 1993. *An Introduction to the Bootstrap*. New York: Chapman & Hall.
- Guinea, G.V., Planas, J. & Elices, M. 1982. Measurement of the Fracture Energy Using Three-Point Bend Tests: 1. Influence of Experimental Procedures. *Mater. Struct.* 25: 212-218.
- Hillerborg, A., Mood er, M. & Petersson, P.E. 1976. Analysis of Crack Formation and Crack Growth in Concrete by Means of Fracture Mechanics and Finite Elements. *Cement Concrete Res.* 6: 773-782.
- Hu, X.Z. & Wittmann, F.H. 1992. Fracture Energy and Fracture Process Zone. *Materials and Structures* 25: 319-326.
- Planas, J. & Elices, M. 1993. Asymptotic Analysis of a Cohesive Crack: 2. Influence of the Softening Curve. *Int. J. Fracture* 64: 221-237.
- Planas, J., Guinea, G.V. & Elices, M. 1997. Generalized Size Effect Equation for Quasibrittle Materials. *Fatigue Fract. Eng. Mater. Struct.* 20(5): 671-687.
- Planas, J., Guinea, G.V. & Elices, M. 1999. Size Effect and Inverse Analysis in Concrete Fracture. *Int. J. Fracture* 95: 367-378.
- Tada, H., Paris, P.C. & Irwin, G.R. 1985. *The Stress Analysis of Cracks Handbook*. Paris Productions, Saint Louis, MO.
- Taini, G. 2002. Determinazione Sperimentale dell'Energia di Frattura del Calcestruzzo. Master Thesis, Politecnico di Milano.